Sun, M., *et al.*: The Impinging Wall Effect on Flame Dynamics and Heat ...
THERMAL SCIENCE: Year 2023, Vol. 27, No. 1B, pp. 855-867

855

THE IMPINGING WALL EFFECT ON FLAME DYNAMICS AND HEAT TRANSFER IN NON-PREMIXED JET FLAMES

by

Meng SUN, Jieyu JIANG, Yongzhe YU, Canxing HE, Kun LIU, and Bin ZHANG*

College of Electromechanical Engineering,
Qingdao University of Science and Technology, Qingdao, China

The impinging jet flame is studied experimentally and numerically accounting for the complex flame-wall interactions in practical combustion devices. Flame dynamics and heat transfer with the effect of impinging wall are analyzed. The 3-D large eddy simulation coupled with detailed chemical reaction mechanism and particle image velocimetry experiment based on cross-correlation measurement principle are performed for verification and further analysis. Results show that vortices are generated due to the Kelvin-Helmholtz instability originated from velocity gradient. The 3-D vortex interactions involving vortex rings and spirals are also indicated by vorticity and the convection of streamwise vorticity is responsible for the effect of vortex spirals associated with turbulent flow transition. In addition, results calculated from four wall thermal conditions are compared and analyzed. Dirichlet condition is inferred to be more suitable for the case of wall materials with higher thermal conductivity. It is indicated that wall thermal condition mainly affects the heat transfer in the near-wall region, but has little effect on the momentum transfer. This study provides references for the adoption of wall conditions in numerical simulation and near-wall treatment in combustion systems.

Key words*: impinging flame, flame dynamics, vortex, wall thermal conditions*

Introduction

Considering the practical combustion systems, such as combustion engines, gas turbine combustors, and other industrial processes, combustion is carried out in a confined or semi-confined space in which flames develop in the vicinity of walls and interact with them. Flame-wall interactions are also occurred in combustion hazards, such as accidental flameout, explosion and fires. In the context of flame-wall interactions, impinging jet flame causes most particular interests in fundamental academic studies because of its higher heat and mass transfer efficiency in the near-wall area, which is related to many practical applications, not only industrial burners, but also metal cutting, glass melting and so on. In order to have a deeper understanding of the jet impinging on the flame, it is necessary to analyze the flow field in the near-wall area and the influence of the wall boundary, especially the thermal boundary condition of the wall.

The impinging flow configuration covers a broad range of important flow phenomena, such as large and small scale vortical structures [1, 2], wall boundary-layers with stagnation, large curvature involving strong shear and normal stresses [3], and wall heat transfer [4]. The

---

* Corresponding author, e-mail: jjieyu2006@163.com

flame-wall interaction has been studied from many aspects. For example, buoyancy-induced vortical structures and the periodic vortex shedding have been well known for decades. It was found that the vortical structures due to buoyancy could affect the flame structure [5-7] and the effect of buoyancy instability on wall heat flux was stronger than that of external disturbance. Pan [8] concluded that the interaction between flame and vortex contained three modes: flame-instability dominated, flow dominated, and a hybrid of the two. The sidewall effects were found to be significant on the flame structure because of the wall-induced vortex deformation [9]. Foucher *et al.* [10] reported the interaction between laminar flame and wall. It was found that the folds of flame front were amplified by fresh gas, and the interaction between flame and wall was easily disturbed by fresh gas. Halouane *et al.* [11] found that a reverse flow occurred within the cavity corner and near the cavity bottom, which interacted with the main flow producing a toroidal swirl close to the jet exit. Geikie *et al.* [12] found that at high turbulence intensities, the baroclinic torque and dilatation decreased, while the magnitude of viscous diffusion increased, and vortex stretching dominated the reacting flow field. Previous studies proof that the flow conditions in the flow field, especially vortex motion, have an important effect on jet flame interacting with an impinging wall. However, research on vortex behavior and development in flow process needs to be supplemented further.

In addition, the wall conditions play important roles in flame-wall interaction. The effect of wall materials on combustion characteristics of flames was studied [13, 14], and results indicated that the higher wall temperature gradient for lower wall thermal conductivity promoted the homogeneous combustion shift upstream and had a wider temperature distribution. Gollapudi *et al.* [15] pointed out that wall temperature was an important parameter in the process of enhanced heat transfer. Tang *et al.* [16] carried out an experimental investigation of the influence of sidewall restraint on flame extension, which found that as the distance from the sidewall to the opening decreased, the longitudinal flame extension length increased, and the transverse flame length decreased. Moreover, the effects of roughness on turbulent flow in the vicinity of wall were investigated. Results indicated that roughness tended to increase the intensity of the velocity and vorticity fluctuations [17], and modified both the shape and magnitudes of the Reynolds stress profiles in the near-wall region [18, 19]. The turbulent flow and heat transfer were numerically studied by Hilo *et al.* [20] and it was pointed out that the heat transfer was increased significantly by the corrugated wall with a backward-facing step. The aforementioned researchers has focused on the influence of wall condition, while more detailed analysis should be presented on the effect of wall thermal condition because of its importance on heat transfer in near-wall region.

The aim of the study is to investigate the flow and combustion dynamics in non-premixed flames with the effect of impinging wall using experimental and numerical methods, and to explore the thermodynamic characteristics at different wall thermal conditions, in order to provide reference for achieving efficient combustion and improving the combustion safety.

## Experimental and numerical methods

Experimental facility

To study the flow dynamics of impinging jet flame, the particle image velocimetry (PIV) experimental apparatus and the measurement set-up have been constructed, which are shown in fig. 1. The experimental system involves two parts: non-premixed combustion system and optical measurement system.

The combustion system is mainly composed of burner, fig. 2, particle mixer, air bottle, fuel bottle and air compressor, which is supplemented by some control devices such as mass-
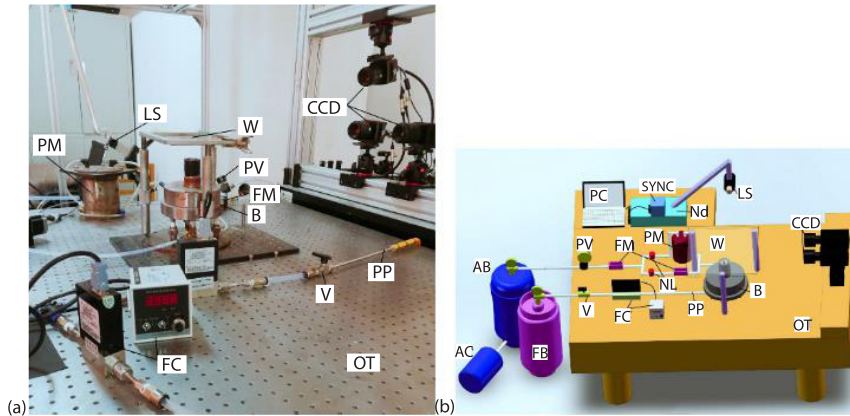
**Figure 1. Diagram of experimental apparatus and measuring apparatus;
(a) experimental schematic, (b) set-up:** *FB – fuel bottle, AB – air bottle,
AC – air compressor, V – valve, PV – pressure-reducing valve, FM – mass-flow meter,
NL – needle valve, FC – mass-flow controller, PM – particle mixer, PP – pipe-line,
W – wall, B – burner, CCD-PIV-CCD – camera, OT – optical table, PC – computer,
SYNC – synchronizer, LS – laser source, Nd-Nd – YAG laser, and TH – thermocouple*

flow meter, needle valve, pressure-reducing valve and mass-flow controller. The supply of fuel and air is firstly introduced. Air is compressed by an air compressor and stored in an air bottle (60 L). The pressurized air is divided into two channels to facilitate the adjustment of tracer particles concentration. One air stream flows out through needle valve and mass-flow meter, and the other is led to the particle mixer, where TiO_2 particles of about 10 μm diameter are provided as tracer particles. After that, the mixture of air and tracer particles flows upward along the circular channel. The CH_4 is stored in fuel bottle (8 L), which flows out through gas valve, mass-flow controller, and then enters the burner. A MF5712-N-200 mass-flow meter and a mass-flow controller with the accuracy of ±7 sccm are used to control mass-flow.
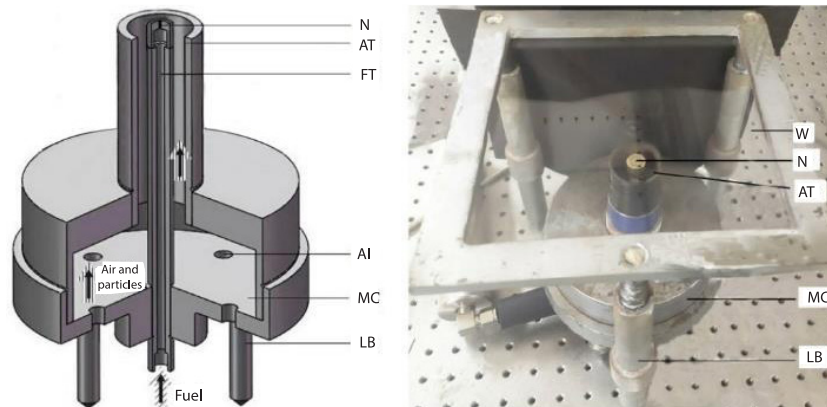
Figure 2. Schematic diagram of burner structure: *AT – air tube, AI – air inlet,
FT – fuel tube, N – nozzle, LB – leveling bolts, MC – the mixing chamber, and W – wall*

The optical measurement system is composed of PIV-CCD camera, double pulse Nd:YAG laser, SYNC-synchronization controller and computer. A 430 mJ/pulse dual-cavity solid-state Nd-YAG laser is used, which has an excitation wavelength of 532 nm. The laser beam

is collimated by a positive lens, and then fanned out on a plane by a cylindrical lens, forming a sheet light with a thickness of 1 mm. A picture of visualized particles image is taken by a Nikon 630090 PowerView 4MP-LS PIV-CCD camera, which has a resolution of 2360 pixels horizontally and 1776 pixels vertically. Each camera contains a 50 mm lenses, a CCD sensor and a 532 ± 5 nm band pass filter. A TSI610036 synchronizer at an accuracy of 1 ns is used to control Nd-YAG laser and trigger PIV-CCD camera to sample at the same time. The time interval between the two frames is 100 μs. The tracer particles in combustor center section are illuminated by the laser, and the particles image information is collected by PIV-CCD camera. Finally, the Insight V3V software is used to process the particle images to obtain the flow field information.

Experimental calibration

To ensure the validation of the experimental results, a calibration procedure is performed before the measurement of experiment. In this process, the calibration plate is placed on a plane parallel to the laser sheet light source above the burner and calibration mode in Insight V3V software is used to calibrate the distance units of the calibration plate with the pixel units of the image acquired by the camera. The key in the adjustment is to ensure that the camera line of sight is perpendicular to the laser sheet light source plane that the distance units of the calibration plate captured by the camera are clearly visible. This can make sure that the reliability of the camera in capturing flow field information and the reliability of Insight V3V software in processing velocity field information.

Numerical implementation

The CH_4 is ejected from the nozzle of 1 mm diameter, d, at the top of burner. Co-flow air nozzle is set as annular tube of 20 mm diameter. An impinging wall with 4 mm thickness is placed 55 mm above the burner. Its density, ρ, is 2160 kg/m³, specific heat capacity, c_p, is 800 J/kgK, and thermal conductivity, λ, is 1.09 W/mK. The size of fluid-flow field is 138 mm × 138 mm × 55 mm. Since the flow field is structurally regular and axisymmetric, half of the analytical object is selected as the calculation domain. The initial velocities of fuel and coflow air are specified as 8 m/s (Re = 469, T = 300 K), 1.1 m/s (Re = 1379, T = 300 K), respectively, which can make sure a non-premixed impinging flame. In addition, velocity-inlet boundary is considered at the inflow, and pressure-outlet boundary is set at the side and outflow of flow field. The non-slip boundary condition is used at the impinging wall. Four wall thermal conditions are considered, respectively in cases 1-4 including Neumann condition which specifies the heat flux value of the top wall, Dirichlet condition which specifies the temperature of the top wall, Robin condition which specifies the surface heat transfer coefficient of the top wall and the temperature of the surrounding air, and the mixed condition of convection with radiation thermal conditions (collectively referred to as Mixed condition in the following). Detailed parameters of four wall thermal conditions are shown in tab. 1. Besides, the value of gravitational acceleration is taken as 9.81 m/s², and the initial temperature and pressure are 300 K and 101 kPa, respectively.

Table 1. Parameters of wall conditions

Case No.	Wall conditions	Parameters
1	Neumann	q = 251.19 W/m²
2	Dirichlet	T_w = 310.3 K
3	Robin	h_{ext} = 10 W/m²K, T_{ext} = 295 K
4	Mixed	h_{ext} = 10 Wm²K, ε_{ext} = 0.94, T_{ext} = 295 K, T_∞ = 295 K

Sun, M., *et al.*: The Impinging Wall Effect on Flame Dynamics and Heat ...
THERMAL SCIENCE: Year 2023, Vol. 27, No. 1B, pp. 855-867

859

In this study, software FLUENT based on the finite volume method is used. The governing equations including faver filtered mass equation, momentum equation, energy equation and transport equation are solved in the simulation, and the details can be found in the previous study [21]. The SIMPLE algorithm is used to enforce mass conservation and to obtain the pressure field by using the relationship between velocity and pressure corrections. The spatial term in the governing equation is discretized by the second-order upwind scheme and the temporal term is discretized by the second-order implicit scheme. Large eddy simulation (LES) with sub-grid model of kinetic-energy transport is employed for turbulence calculations [22, 23]. Non-premixed combustion model based on the steady diffusion flamelet model and the statistical PDF methods are used to solve the mutual effect of combustion and turbulence [24, 25], which is combined with GRI-Mech 3.0 chemical reaction mechanism [26]. The discrete ordinates (DO) radiation model is applied for calculating radiation [27].

According to the structure of the combustor, the calculation domain is meshed into hexahedral unstructured grids. In order to accurately capture the characteristics of the flow field, a boundary-layer with a thickness of about 3.96 mm is used to refine the mesh near the wall. The initial height of the boundary-layer row is 0.1 mm, which gradually increases with a growth factor of 1.2, and the number of rows is 12. Four grid cases are used for independence test, and the results are shown in fig. 3. The temperature distributions along the jet center in four grid cases show that results using 1 million and 1.5 million grid points are almost the same, but some different distributions of calculation results between 0.25 million and 0.5 million grid points can be observed. So 1 million grid points are sufficient to accurately resolve the physical problem by avoiding the excessive computational cost.
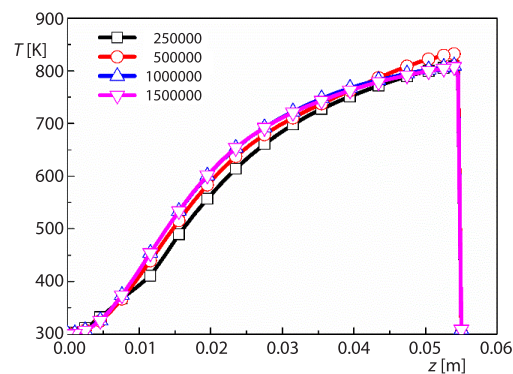

Figure 3. Temperature distributions on the center line at different mesh densities

## Results and discussions

Comparison and verification

Figure 4 shows the comparison of time averaged axial velocity and radial velocity between the PIV results and LES calculation data on $z = 0.01$ m, 0.03 m, and 0.05 m. Since better symmetry is observed after the flow field is fully developed, half of the entire flow field is selected for comparison during the comparison process. It can be seen that the numerical simulation data are in good agreement with the PIV experiment results. The numerical simulation data show two peak values corresponding to the fuel jet and coflow air, respectively, which is consistent with the PIV experiment results. The direction and magnitude of the radial velocity in the PIV experiment and numerical simulation are also well matched.

Flame dynamics analysis

Figures 5 and 6 represents the spatial distributions, figs. 5(a)-5(d), and velocity vectors, figs. 6(a)-6(d) of tracer particles in non-premixed impinging flame, respectively. It is noticed that some small-scale vortical structures indicated by the tracer particles bulges are generated at the interface of coflow and ambient air in fig. 5. The presence of vortex leads to the stretching and compression behaviors at the interface, and tracer particles are pushed outward,
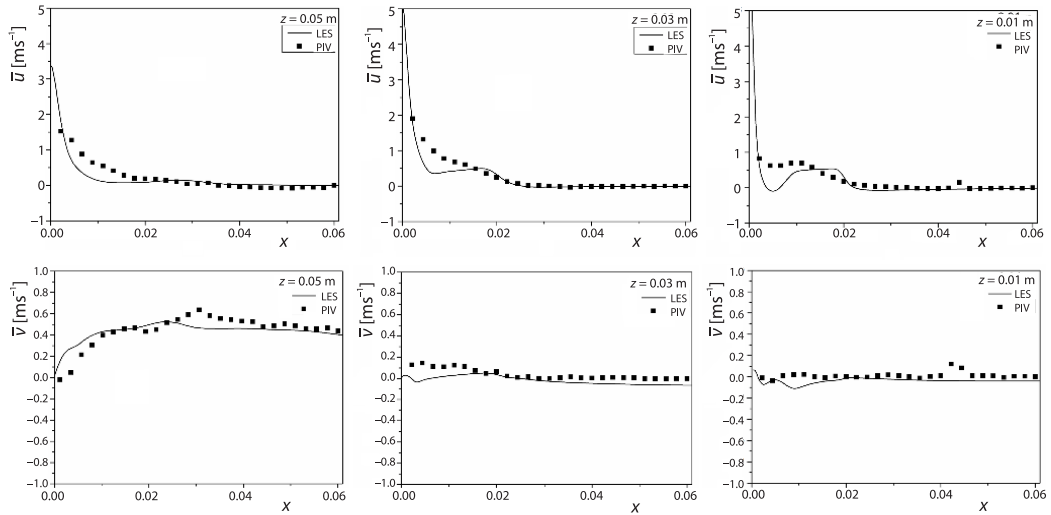
Figure 4. Comparison and verification of time averaged axial velocity $\bar{u}$ and radial velocity $\bar{v}$ between experiment results and numerical simulation data
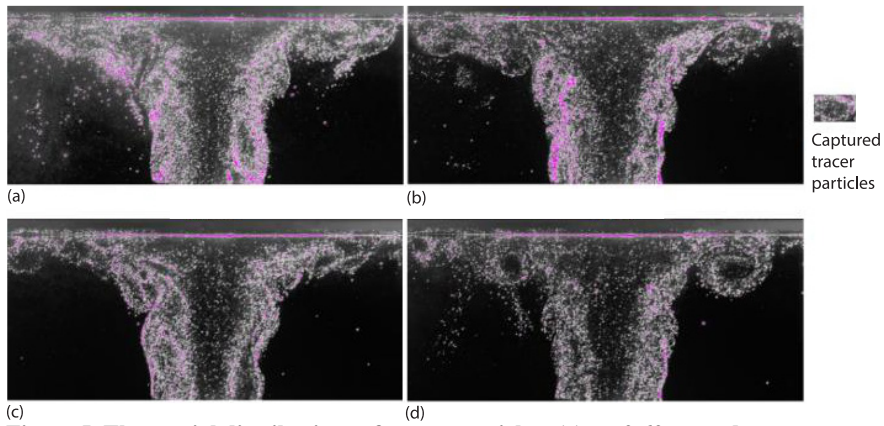
Figure 5. The spatial distributions of tracer particles; (a) t = 0.60 seconds, (b) t = 0.90 seconds, (c) t = 1.20 seconds, and (d) t = 1.50 seconds
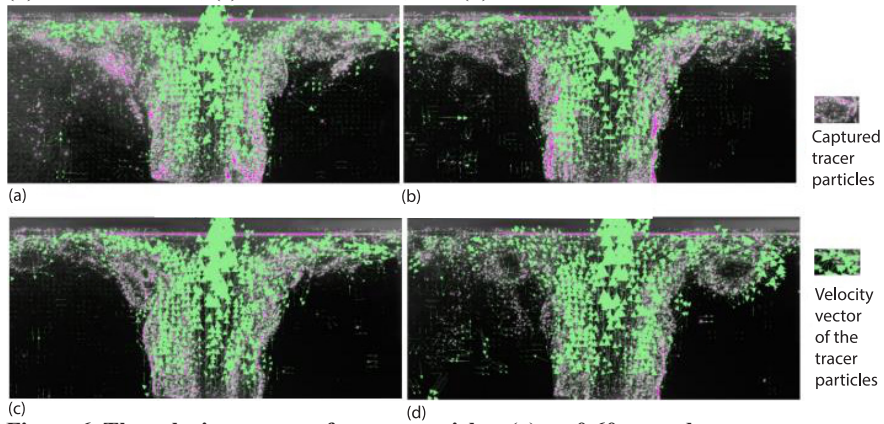
Figure 6. The velocity vectors of tracer particles; (a) t = 0.60 seconds, (b) t = 0.90 seconds, (c) t = 1.20 seconds, and (d) t = 1.50 seconds

resulting in a wider distribution region and an irregular interface. As shown in the snapshots of velocity vectors of tracer particles in fig. 6, the velocity vector distribution of tracer particles is also irregular, and small-scale vortical structures are demonstrated at the interface of coflow with ambient air, while the parallel motion of tracer particles is illustrated at the fuel jet center. It can be inferred that the tracer particles at the junction are affected by shear stress originated from the velocity gradient between coflow and ambient air.

It is noticed that the large-scale vortical structures are formed in the near-wall region. After reaching the near-wall region, the impinging jet flame spreads along the wall surface in the spanwise direction that forms the wall boundary-layer. It is found that the velocity vector of tracer particles is chaotic, and large-scale vortical structures are presented at the outside of wall boundary-layer. It can be attributed to the existence of Kelvin-Helmholtz instability and the coupling effect of turbulence and wall. Large velocity gradient at the boundary of coflow leads to a large shear stress, resulting in Kelvin-Helmholtz instability. Tracer particles in near-wall region are subjected to strong shear and normal stresses during the movement, thus causing the change of flow direction. In addition, it is worth noting that the small-scale vortices in fig. 6(a) gradually become stronger and bigger downstream, and evolve into larger-scale vortical structures in fig. 6(d) in the near-wall region. It is indicated that there might be vortex pairing/merging downstream. A large heading vortex at the end of wall boundary-layer is consequently generated in fig. 6(d).

According the data of simulation and experiment, CH_4 is ejected from the nozzle and quickly completes the turbulent transition and hits the wall under the action of coflow air, after which the flow gradually develops into a stable state. The instantaneous velocity vector distributions are shown in figs. 7 and 8, where results, figs. 7(a)-7(d) are demonstrated from experimental data and results figs. 8(a)-8(d) are obtained from numerical calculation. The non-premixed flame is initially formed in the primary jet stream, and propagated towards the impinging wall. Then, it is deflected from the wall and convected along the surface of impinging wall after the impingement of wall. Upon impingement, the streamwise velocity of jet decays to a zero value. So the flow field can be divided into three main regions: the primary jet region (R1), the wall jet region (R2) and the low speed stagnation region (R3), which is consistent with the findings of Subhash and Anjan [28].

As illustrated in fig. 7, the velocity distribution is irregular at the outer side of the primary jet region, where small-scale vortices (such as vortices A2 and A4), and large-scale vortical structures (such as vortices B1-B4 and C1-C4) are displayed. In addition, the air-flow velocity in the primary jet region is greater than that in wall jet region, which can be attributed to the momentum loss caused by the impingement. The velocity difference at the junction of different regions can lead to the formation of shear stresses, which causes the flow to fluctuate and generate the vortical structure.

Vortex dynamics can be illustrated by examining the vorticity transport. The vorticity contours in *x*-direction at $z = 0.022$ m in fig. 9(a) and $z = 0.044$ m in fig. 9(b) are shown, where vorticity is mainly demonstrated in the interface of fuel jet, coflow and ambient air. The aforementioned rotation direction of vortex rings is further presented by the positive and negative values of vorticity. It is confirmed the counter-rotating vortices are formed, which are specified by the opposite signs of vorticity. Compared with fig. 9(a), it can be observed that the vorticity distribution in the primary jet region is wider and farther away from the fuel jet center in fig. 9(b), which is attributed to the vortex motion downstream. The positive-negative-positive (or negative-positive-negative) distributions of vorticity are observed, which indicate the convection of streamwise vorticity. It can be inferred that the development of streamwise vorticity
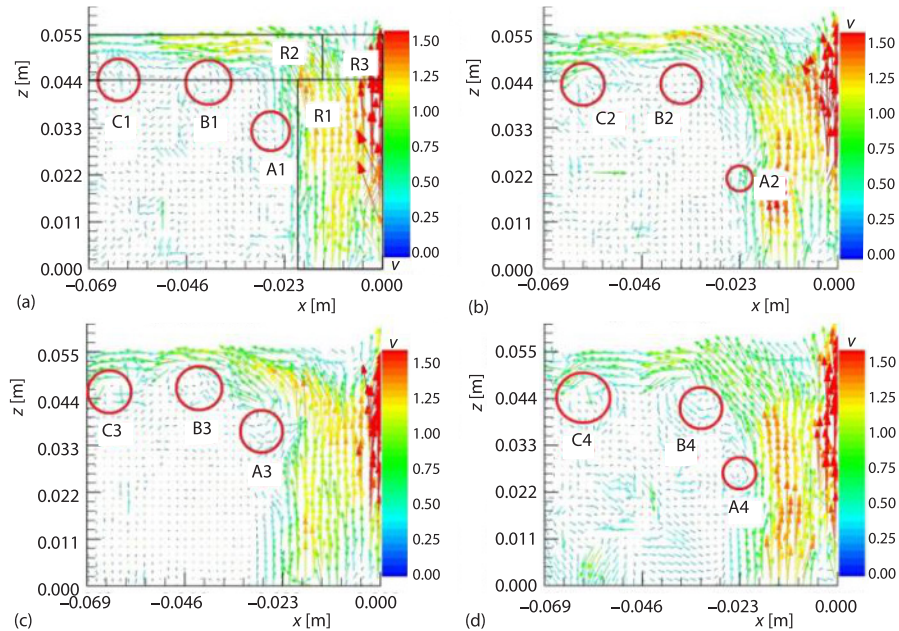
**Figure 7. Experimental results of velocity vector (R1 – the primary jet region,
R2 – the wall jet region, R3 – the low speed stagnation region; (a) *t* = 0.60 seconds,
(b) *t* = 0.90 seconds, (c) *t* = 1.20 seconds, and (d) *t* = 1.50 seconds**
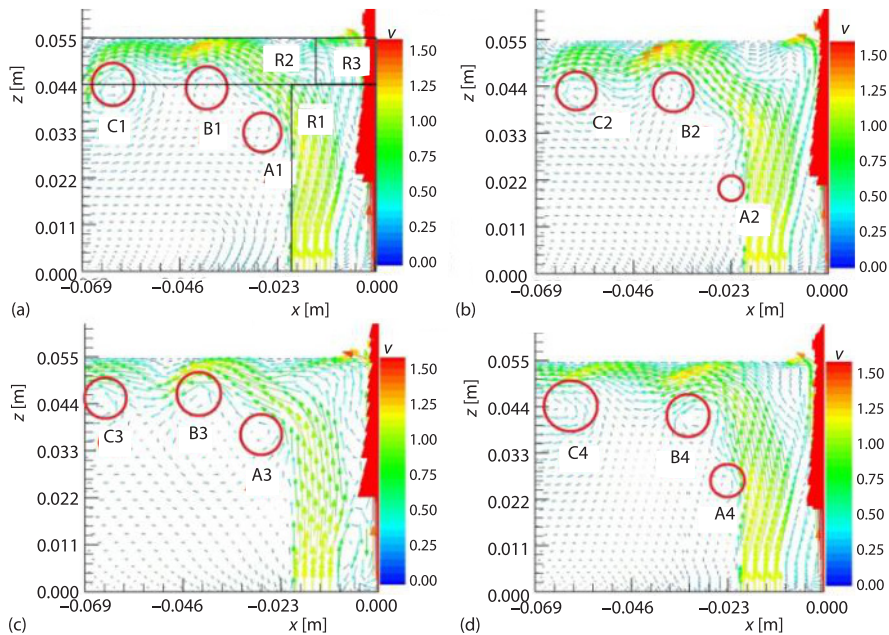
**Figure 8. Numerical results of velocity vector, R1 – the primary jet region,
R2 – the wall jet region, R3 – the low speed stagnation region; (a) *t* = 0.60 seconds,
(b) *t* = 0.90 seconds, (c) *t*=1.20 seconds, and (d) *t* = 1.50 seconds**

Sun, M., *et al.*: The Impinging Wall Effect on Flame Dynamics and Heat ...
THERMAL SCIENCE: Year 2023, Vol. 27, No. 1B, pp. 855-867

863

leads to the breakdown of vortical structures due to strong vortex interactions involving vortex rings and spirals, which is associated with the turbulent flow transition. The 3-D vortex interactions are associated with the flame instability. The flow and combustion instability may consequently result in the combustion safety problem.
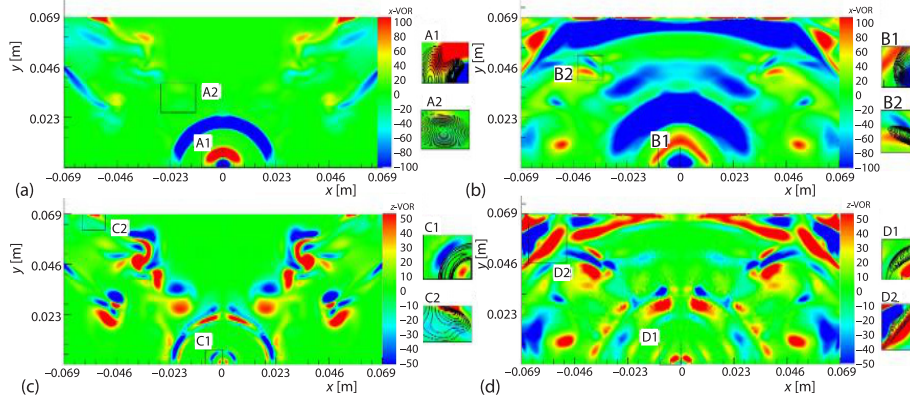

**Figure 9. Vorticity (VOR) in *x*-direction at *z* = 0.022 m (a) and *z* = 0.044 m (b),
and *z*-direction at *z* = 0.022 m (c) and *z* = 0.044 m (d)**

Effects of wall thermal conditions

The flow field in the vicinity of wall is inevitably affected by the wall heat transfer process and the wall thermal condition is of great importance to the heat transfer in near-wall region. In this section, four wall thermal conditions are adopted, respectively to explore the effect of wall, including Neumann condition, Dirichlet condition, Robin condition, and Mixed condition. The detailed parameters at the wall are shown in tab. 1.
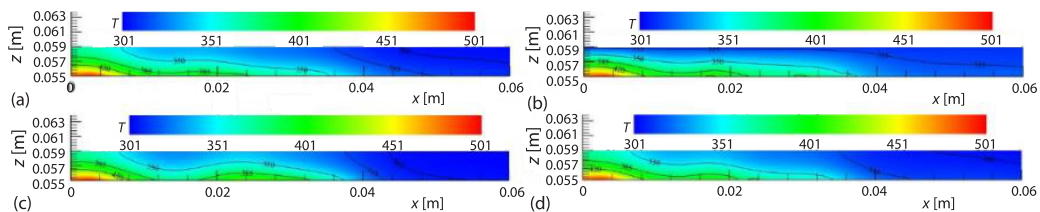
Figure 10(a) shows temperature distribution at bottom wall (*y* = 0 m, *z* = 0.055 m). For the bottom wall temperature in Neumann condition, Dirichlet condition, and Mixed condition, the overall distribution trend is similar, but there are large fluctuations in Robin condition case in the 0.010-0.035 m region. Figure 10(b) presents temperature distribution at top wall (*y* = 0 m, *z* = 0.059 m). Large discrepancy can be observed between experimental results and simulation in Dirichlet condition case. It can be attributed to the uniform wall temperature and no temperature fluctuation in Dirichlet condition case. In the region of 0.01-0.03 m, the top wall
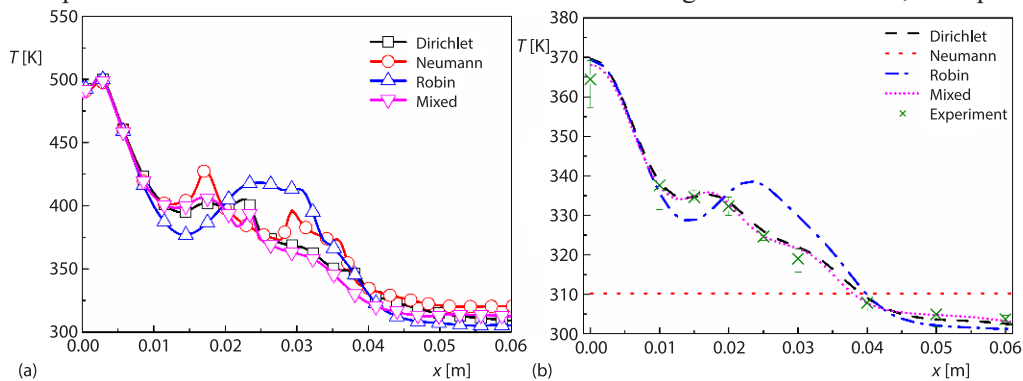
**Figure 10. Distributions of temperature at the bottom (a) and top (b) wall (*y* = 0 m) in
different wall thermal condition cases**

864

Sun, M., *et al.*: The Impinging Wall Effect on Flame Dynamics and Heat ...
THERMAL SCIENCE: Year 2023, Vol. 27, No. 1B, pp. 855-867

temperature in Robin condition case fluctuates greatly, which can be attributed to that the influence of heat convection is greater than other heat transfer modes in this work condition. Similar distribution of top wall temperature characteristics can be observed in Neumann condition and mixed condition cases. Moreover, results in mixed condition case are in good agreement with the experimental measurements with a maximum relative error of 1.65%.

Figure 11 represents the wall temperature distributions in x-z plane in different wall thermal condition cases. Noted that in the central region of jet impact ($z < 0.008$ m), the distribution of high temperature region ($T > 420$ K) is almost the same under four wall thermal conditions except for a larger temperature gradient in Dirichlet condition. The area where the impacted wall is directly opposite the nozzle is called the stagnation area, where the local heat transfer intensity is the highest in the actual heat transfer process, and the main heat transfer mode is heat conduction, which means that the heat transfer rate inside the wall is mainly affected by the wall material. However, the Dirichlet condition fixes the temperature of the top wall to 310.3 K, which causes a larger temperature gradient than other three conditions near the top wall. It can be inferred that the larger the thermal conductivity of the wall material, the smaller this temperature gradient will be, and the closer the results in Dirichlet condition case will be to those in other thermal condition cases, which means that Dirichlet condition is applicable to the case of high thermal conductivity of wall material.

Figure 11. Wall temperature distributions in x-z plane in different wall thermal condition cases; (a) Neumann condition, (b) Dirichlet condition, (c) Robin condition, and (d) mixed condition

Figure 12 shows the distributions of temperature in the near-wall region ($z = 0.04$-0.055 m). Result of numerical simulation in Robin condition and mixed condition case shows that the temperature distribution in near-wall region is relatively flat towards the wall, while the range of high temperatures in stagnation area in Neumann condition case is wider and a distinct temperature islands can be observed in Dirichlet condition case. Neumann
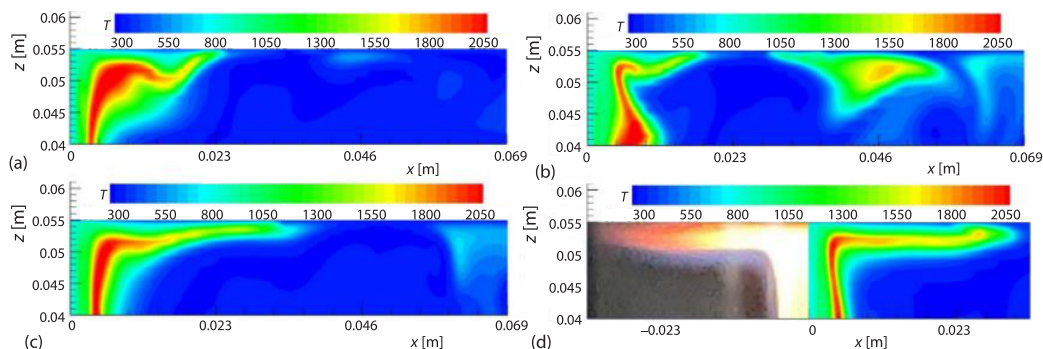
Figure 12. Temperature distributions in the near-wall region ($z = 0.04$-0.055 m) in different wall thermal condition cases; (a:) Neumann condition, (b) Dirichlet condition, (c) Robin condition, and (d) mixed condition

condition sets the heat flux to a fixed value and the highest local heat transfer intensity in stagnation area means a larger heat flux than the fixed value in Neumann condition case. The small fixed value heat flux results in a smaller local heat transfer than the actual case and the range of high temperature in stagnation area becomes wider. That means Neumann condition is not suitable for the operation condition with high local heat flux and local heat transfer analysis in this working condition. The reason of temperature islanding in Dirichlet condition case is the discontinuity of flame because of the flame quenching. Dirichlet condition fixed the top wall temperature into a fixed value causing a sharp temperature gradient, which means a high heat loss. Wall quenching can be also observed in near-wall region which is associated with efficient combustion. Similar as the Neumann condition, the local temperature is much higher than the wall, and the Dirichlet condition is not suitable in this respect. The result in mixed condition case shows good consistency with the experiment data, which means the mixed condition can be the most applicable condition regardless of the cost of simulation.

Figure 13 shows the distribution of velocity in the near-wall region in different wall thermal condition cases. It is found that the distribution of velocity in the wall jet region is almost same under the four wall thermal conditions. Compared with fig. 13, the difference of temperature distribution showed in fig. 12 under different wall conditions is more obvious, but the difference of velocity distribution in different wall thermal condition cases is much weaker. It means that different wall thermal conditions mainly affect the heat transfer in the near-wall region, but much less affect the momentum transfer. The differences of velocity distribution in four wall thermal condition cases are mainly concentrated in the stagnation region with different velocity gradient. It is speculated that different wall thermal conditions affect the heat transfer in the stagnation zone, resulting in different fuel-air convection conditions and that leads to different velocity distributions.
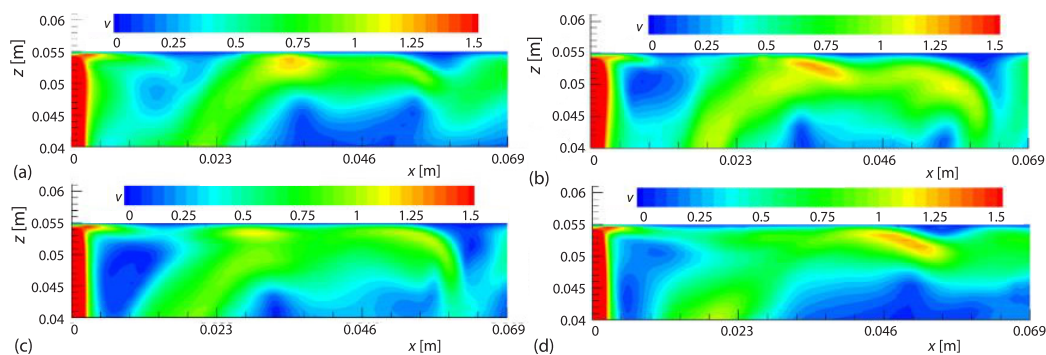
Figure 13. Distributions of velocity in the near-wall region in different wall thermal condition cases;
(a) Neumann condition, (b) Dirichlet condition, (c) Robin condition, and (d) mixed condition

Conclusions

The non-premixed impinging flames are carried out using PIV and LES methods. The flame dynamics and heat transfer with the effect of impinging wall are analyzed emphatically and concluded as followings.

- Vortex is easily found at the interface of the primary jet region (R1), the wall jet region (R2), and the low speed stagnation region (R3) due to the Kelvin-Helmholtz instability. The small-scale vortices are generated at the interface of the coflow air and the ambient air leading to the stretching and compression behaviors. Large-scale vortical structures are formed in the near-wall region.

- It is noticed that 3-D vortex interactions involving vortex rings and spirals occur in the flow field. The counter-rotating vortices are also formed and spread downstream. Moreover, the effect of vortex spirals is demonstrated by the convection of streamwise vorticity. Turbulent flow transition is mainly associated with the breakdown of vortical structures due to strong vortex interactions involving vortex rings and spirals.
- Wall thermal condition affects flow dynamics and thermodynamic characteristics of the impinging jet flames in the vicinity of wall. It is found that Neumann condition and Dirichlet condition are not applicable for the local heat conduction analysis. Dirichlet condition is inferred to be more suitable for the case of wall materials with higher thermal conductivity. Results in Mixed condition case are more consistent with the experiment results. It can be also inferred that the wall thermal condition mainly acts on the heat transfer in the near-wall region, while it has less effect on the momentum transfer.

Acknowledgment

Nomenclature

c_p – specific heat capacity, [Jkg^{-1}K^{-1}]
d – diameter, [m]
h – heat transfer coefficient, [Wm^{-2}K^{-1}]
q – wall heat flux, [Wm^{-2}]
Re – Reynolds number (= $\rho vd/\mu$), [–]
T – temperature, [K]
$\bar{u}$ – time averaged axial velocity, [ms^{-1}]

VOR – vorticity, [s^{-1}]
$\bar{u}, \bar{v}$ – time averaged axial and radial velocity, [ms^{-1}]

Greg symbols

λ – thermal conductivity, [Wm^{-1}K^{-1}]
μ – dynamic viscosity, [Pa·s]
ρ – density, [kgm^{-3}]

References

[1] Jiang, X., *et al.*, Direct Numerical Simulation of a Non-Premixed Impinging Jet Flame, *Journal of Heat Transfer-Transactions of the ASME, 129* (2007), 8, 951
[2] Maruta, K., Micro and Mesoscale Combustion, *Proceedings of the Combustion Institute, 33* (2011), 1, pp. 125-150
[3] Janetzke, T., *et al.*, Time Resolved Investigations on Flow Field and Quasi Wall Shear Stress of an Impingement Configurati on with Pulsating Jets by Means of High Speed PIV and a Surface hot Wire Array, *International Journal of Heat and Fluid-flow, 30* (2009), 5, pp. 877-885
[4] Xu, S. T., *et al.*, Effects of Wall Temperature on Methane MILD Combustion and Heat Transfer Behaviors with Non-Preheate Air, *Applied Thermal Engineering, 174* (2020), 25, 115282
[5] Ranga Dinesh, K. K. J., *et al.*, Analysis of Impinging Wall Effects on Hydrogen Non-Premixed Flame, *Combustion Sciences and Technology, 184* (2012), 9, pp. 1244-1268
[6] Jiang, J. Y., *et al.*, A Study of Instabilities in Hydrogen-Air Impinging Jet Flames Using Two and 3-D Direct Numerical Simulations, *Energy Procedia, 66* (2015), Dec., pp. 325-328
[7] Zhang, X. L., *et al.*, Experimental Study on Flame Morphologic Characteristics of Wall Attached Non-Premixed Buoyancy Driven Turbulent Flames, *Applied Energy, 254* (2019), 113672
[8] Pan, K. L., Flame Propagation with Hydrodynamic Instability in Vortical Flows, *Journal of Mechanics, 24* (2008), 3
[9] Jiang X., *et al.*, Dynamics and Structure of Transitional Buoyant Jet Diffusion Flames with Side-Wall Effects, *Combustion and Flame, 133* (2003), 1-2, pp. 29-45
[10] Foucher, F., *et al.*, Flame Wall Interaction: Effect of Stretch, *Experimental Thermal and Fluid Science, 27* (2003), 4, pp. 431-437
[11] Halouane Y., *et al.*, Turbulent Heat Transfer for Impinging Jet Flowing Inside a Cylindrical Hot Cavity, *Thermal Science, 19* (2015), 1, pp.141-154
[12] Geikie M. K., *et al.*, Turbulent Flame-Vortex Dynamics of Bluff-Body Premixed Flames, *Combustion and Flame, 223* (2021), Jan., pp. 28-41

Sun, M., *et al.*: The Impinging Wall Effect on Flame Dynamics and Heat ...
THERMAL SCIENCE: Year 2023, Vol. 27, No. 1B, pp. 855-867

867

[13] Yan, Y. F., *et al.*, Numerical Study of Effect of Wall Parameters on Catalytic Combustion Characteristics of CH4/Air in a Heat re-Circulation Micro-Combustor, *Energy Conversion and Management*, *118* (2016), 15, pp. 474-484

[14] Chen, G. B., *et al.*, Effects of Catalytic Walls on Hydrogen/Air Combustion Inside a Micro-Tube, *Applied Catalysis A-General*, *332* (2007), 1, pp. 89-97

[15] Gollapudi, L., *et al.*, Heat Enhancement Analysis of a Differentially Heated Inclined Square Enclosure Filled with Al_2O_3 Nanofluids under Three Base Fluids: Water, Water-Ethylene Glycol Mixture and Ethylene Glycol, *Thermal Science*, *25* (2021), 6A, pp. 4383-4393

[16] Tang, F., *et al.*, Effect of Sidewall on the Flame Extension Characteristics Beneath a Ceiling Induced by Carriage Fire in a Channel, *Combustion and Flame*, *223* (2021), 4, pp. 202-215

[17] Bhaganagar, K., *et al.*, Effect of Roughness on Wall-Bounded Turbulence, *Flow Turbulence and Combustion*, *72* (2014), 2-4, pp. 463-492

[18] Rostamy, N., *et al*., The Effect of Surface Roughness on the Turbulence Structure of a Plane Wall Jet, *Physics of Fluids*, *23* (2011), 8, 5

[19] Essel, E. E., *et al.*, Roughness Effects on Turbulent Flow Downstream of a Backward Facing Step, *Flow Turbulence and Combustion*, *94* (2015), 1, pp. 125-153

[20] Hilo, A. K., *et al.*, Effect of Corrugated Wall Combined with Backward-Facing Step Channel on Fluid-Flow and Heat Transfer, *Energy*, *19*0 (2020), 1, 116294

[21] Li H., *et al.*, A Study of the Influence of Coflow on Flame Dynamics in Impinging Jet Diffusion Flames, *Journal of Turbulence*, *22* (2021), 8, pp. 461-480

[22] Adamczyk, W. P., *et al.*, Application of LES-CFD for Predicting Pulverized-Coal Working Conditions after Installation of NO_x Control System, *Energy*, *160* (2018), 1, pp. 693-709

[23] Payri, R., *et al.*, The Potential of Large Eddy Simulation (LES) Code for the Modelling of Flow in Diesel Injectors, *Mathematical and Computer Modelling*, *52* (2010), 7-8, pp. 1151-1160

[24] Pierce, C. D., *et al.*, Progress-Variable Approach for Large-Eddy Simulation of Non-Premixed Turbulent Combustion, *Journal of Fluid Mechanics*, *50*4 (2004), 1, pp. 73-97

[25] Peters N., Laminar Diffusion Flamelet Models in Non-Premixed Turbulent Combustion, *Progress in Energy and Combustion Science*,*10* (1984), 3, pp. 319-339

[26] Smith, G. P., *et al.*, GRI-Mech 3.0. http://www.me. berkeley.edu/gri_mech/, 1999

[27] Tu, Y. J., *et al*., Numerical Study of H_2O Addition Effects on Pulverized Coal Oxy-MILD Combustion, *Fuel Processing Technology*, *138* (2015), Oct., pp. 252-262

[28] Subhash, C., *et al.*, Flame Impingement Heat Transfer: A Review, *Energy Conversion and Management*, *46* (2005), 18-19, pp. 2803-2837